

A Computer Model of Engineered Cardiac Monolayers

Jong M. Kim,* Nenad Bursac, and Craig S. Henriquez

Department of Biomedical Engineering, Duke University, Durham, North Carolina

ABSTRACT Engineered monolayers created using microabrasion and micropatterning methods have provided a simplified *in vitro* system to study the effects of anisotropy and fiber direction on electrical propagation. Interpreting the behavior in these culture systems has often been performed using classical computer models with continuous properties. However, such models do not account for the effects of random cell shapes, cell orientations, and cleft spaces inherent in these monolayers on the resulting wavefront conduction. This work presents a novel methodology for modeling a monolayer of cardiac tissue in which the factors governing cell shape, cell-to-cell coupling, and degree of cleft space are not constant but rather are treated as spatially random with assigned distributions. This modeling approach makes it possible to simulate wavefront propagation in a manner analogous to performing experiments on engineered monolayer tissues. Simulated results are compared to previously published measured data from monolayers used to investigate the role of cellular architecture on conduction velocities and anisotropy ratios. We also present an estimate for obtaining the electrical properties from these networks and demonstrate how variations in the discrete cellular architecture affect the macroscopic conductivities. The simulations support the common assumption that under normal ranges of coupling strength, tissues with relatively uniform distributions of cell shapes and connectivity can be represented using continuous models with conductivities derived from random discrete cellular architecture using either global or local estimates. The results also reveal that in the presence of abrupt changes in cell orientation, local estimates of tissue properties predict smoother changes in conductivity that may not adequately predict the discrete nature of propagation at the transition sites.

INTRODUCTION

The anisotropy in electrical properties arising from the distribution and coupling of cardiac cells in tissue has been shown to have a significant impact on impulse initiation and propagation (1–5). Changes in anisotropy often arise in certain cardiac pathologies such as ischemia, infarction, and heart failure (6–8). This change is usually related to altered gap junction distribution and/or expression, and the formation of collagenous septa between the cardiac fibers and groups of cells that result in discontinuous transverse propagation (9). Although it is known that the type, amount, and distribution of gap junctions in the cell membrane, the cell size and geometry, and the interconnectivity of cells determine the magnitude of anisotropy of tissue, studying the separate effects of each of these factors experimentally has been challenging (1,5).

Recent advances in tissue engineering and micropatterning techniques have made it possible to create monolayers in which the degree of anisotropy can be reproducibly controlled. Bursac et al. presented an *in vitro* model system that enables systematic manipulation of the degree, orientation, and nonuniformity (continuity) of anisotropy in centimeter-sized monolayer cultures of neonatal rat cardiac myocytes (1). Using micropatterning, they cultured series of cardiac monolayer tissues whose microscale continuity changes from discontinuous to continuous and whose cell orientations change from oriented (anisotropic) to disoriented (isotropic).

Although these experimental monolayers allow for sophisticated electrophysiological, pharmacological, and genetic studies of simple impulse propagation and reentry dynamics *in vitro*, they are currently limited to neonatal cells with electrophysiological properties that differ from those of humans. In addition, some features of the tissue, like the magnitude and distribution of gap junctions, are not easy to control locally.

Another approach for studying the impact of tissue cellular structure on conduction is to make use of computer models (4,5,10–12). Many models of cardiac tissue assume continuous properties, where the electrical properties are usually assigned to match the observed macroscopic conduction velocities in the tissue and account for macroscopic variations in fiber orientation (13–15). Another approach to model cardiac tissue is to explicitly represent the coupling between cells or fibers. Leon et al. presented a discrete cable model connected with a regular array of identical resistors such that the discontinuity of the tissue only appeared in the transverse direction (11). This approach has been extended to consider more complex anisotropy (16). Spach et al. modeled a tissue as individual cells whose cell boundaries were duplicated from isolated cardiac cells and in which the gap junctions were arranged to approximate the experimental observations (4). In the coupled cable approach, the cell shapes have been idealized to be cylindrical, limiting the random variation in cell size and coupling observed in native tissue. In the models used by Spach et al., the shape of the cell is constrained to map to a rectangular Cartesian grid, limiting the ability to study the effects of random cell orientations.

Submitted July 2, 2009, and accepted for publication January 5, 2010.

*Correspondence: jongmyeong.kim@gmail.com

Editor: Peter C. Jordan.

© 2010 by the Biophysical Society
0006-3495/10/05/1762/10 \$2.00

doi: 10.1016/j.bpj.2010.01.008

Although simulations of the discrete models of Spach et al. have revealed that changes in cell size and in distribution and coupling strength of gap junctions can influence conduction velocity, the relationship of these changes in tissue structure to the macroscopic conductivity has not been fully elucidated (17). One of the challenges is that it is not always clear how to obtain the effective conductivities in multidimensional discrete tissue with random structure that involves variations in cell shape, orientations, and coupling. In this article, we present a novel approach to modeling discrete cardiac tissue in which the factors governing cell shape, cell-to-cell coupling, and the degree of cleft space are not constant but rather are spatially random with assigned distributions. Using this approach, it is possible to construct a number of random cellular networks that have different tissue features yet possess statistically similar macroscopic behavior. By creating several realizations of the same tissue, it is possible to perform simulations in a manner analogous to that used in experiments performed on engineered tissue with natural variations from monolayer to monolayer. We also present a global and a local approach to obtain the macroscopic conductivities from these random networks. The simulations reveal that under normal ranges, global changes in cell shape and connectivity are manifested as changes in the effective macroscopic intracellular tissue conductivities that result in differences in both the macroscopic conduction velocities and the conduction velocity anisotropy ratios. The results show that over a normal range of parameters, a continuous model with appropriately assigned conductivities can explain measured conduction velocities in discrete cardiac tissue with complex microstructure. The variance of the global estimates, however, increases with increasing degree of discreteness (i.e., cleft space). The results also reveal that in the presence of abrupt changes in cell orientation, local estimates of the conductivities predict smoother changes in conductivities that may not adequately predict the discrete nature of propagation at the transition sites.

METHODS

Generation of discrete tissue pattern

The simulated tissue was generated by 1), defining template cells; 2), modifying the cell shapes; and 3), adding clefts (Fig. S1, A–C, in the [Supporting Material](#)). The tissue domain was populated with nonoverlapping elliptical template cells with assigned orientations and locations. To accomplish this, a template cell of 120 μm in length and 24 μm in width was first generated at the top right of the domain. This cell was moved toward the bottom left until it could no longer move due to the presence of other cells or the boundaries of the domain. Upon placement, each template cell was rotated with an angle drawn randomly from a normal distribution, thus controlling the alignment of the cells in the tissue. This process was repeated until the domain was filled with the template cells. Once the template cells filled the domain, cell shapes were modified to fill the gaps between cells. A cell was selected in random order and the boundary of this cell was expanded, by moving randomly selected boundary points away from the cell center by a small amount without overlapping with neighboring

cells. This expansion was repeated several times for all the cells in the tissue, with simultaneous gradual reduction in the amount of expansion. Finally, clefts were incorporated in the tissue by shrinking the width of randomly selected cells. To accomplish this step, each cell was assigned a random number drawn from a uniform distribution between 0 and 1. Cells whose assigned random numbers were smaller than cleft probability were selected to be reduced in size. The selected cell was reduced by moving each boundary point toward the cell's longitudinal line, which passes through the cell center in the length direction. The resulting tissue contained random-shaped cells whose orientations followed the orientations of the templates. The cell orientation was controlled by the standard deviation of the normal distribution, whereas the amount of cleft space was controlled by cleft probability.

Effective tissue conductivity measure

Two methods (global and local) were used to estimate the effective conductivity of the intracellular space. In the global method, the membrane elements were removed, leaving only the passive intracellular network that contained both the intracellular space of the cells and the coupling conductance between cells. This method is also referred to as the equivalent circuit method. For regularly arranged cells, the effective conductivity can be obtained analytically. For example, if the tissue is composed of rectangular cells that are stacked on top of each other with uniform width, W , and length, L , and if gap couplings are uniform along the cell borders with a coupling strength/unit contact area given by g , then the effective tissue conductivity can be written as

$$\sigma_L = \frac{Lg\sigma}{Lg + \sigma} \quad (1)$$

$$\sigma_T = \frac{Wg\sigma}{Wg + \sigma}, \quad (2)$$

where σ , σ_L , and σ_T are intracellular conductivity, longitudinal tissue conductivity, and transverse tissue conductivity, respectively. For tissues with irregularly shaped cells and connectivity, a numerical approach can be used to obtain the effective properties. To accomplish this, cells at one edge of the tissue were grounded and current was injected into the cells at the other edge through discrete current sources. The potential was measured through the tissue and the total injected current was measured by summing up all the discrete sources. This measured potential was then used to estimate the electrical field strength, E , defined as the negative gradient of potential, by performing a linear fit of the potential and the distance from the current source.

$$V = -Ex + b. \quad (3)$$

The effective conductivity, σ , was estimated by the ratio between current flux and electrical field strength:

$$\sigma = J/E, \quad (4)$$

where current flux, J , was obtained from the sum of the injected current divided by the cross-sectional area of the tissue. This method was independently applied in the longitudinal and transverse directions to obtain the conductivities in each direction.

A local method for estimating the effective intracellular conductivity was also developed. In principle, this method can be experimentally implemented. This method consisted of two steps: 1), estimating passive membrane resistance, R_m , from the transmembrane potential of an isolated cell subject to a subthreshold stimulus; and 2), estimating effective tissue conductivity from the steady-state membrane potential. In the first step, the passive membrane resistance, R_m , was estimated from the measured subthreshold time response from a single, isolated cell from the model using simple resistor-capacitor circuit analysis.

$$V = V_0 + (V_S - V_0) \exp\left(-\frac{t}{R_m C_m}\right), \quad (5)$$

where V_0 and V_S are the initial and steady-state potentials, respectively. Under the assumption that the membrane capacitance, C_m , is $1 \mu\text{F}/\text{cm}^2$, the membrane resistance, R_m , was estimated from this equation and the measured time response of the membrane potential. In the second step of this method, the subthreshold point stimulus was applied at the center of the discrete tissue. If the stimulus pulse is long enough, the membrane capacitance is assumed to be fully charged at steady state. The steady-state membrane potential of the discrete tissue was compared with that of the continuous tissue, with the membrane replaced by R_m and with conductivity systemically changed to minimize the error between the steady-state membrane potential obtained from the discrete tissue and that obtained from the continuous tissue. The longitudinal and transverse conductivities of the continuous tissue model minimizing this error were considered to be the corresponding effective conductivities of the discrete tissue model. The Levenberg-Marquardt algorithm was used for the numerical estimation (18). This method is also referred to as the subthreshold response method.

Numerical and computational methods

Because of the computational efficiency, the membrane kinetics were described with the model proposed by Bueno-Orovio and colleagues (the Bueno-Orovio-Cherry-Fenton-Karma model) (19), based on the model initially published by Fenton and Karma (FK) (20) with parameters in Table S1 fit to match the Wang-Sobie (WS) model (21) of a neonatal mouse cell, which has a shape and a duration that resemble those of neonatal rat cells. These parameters were found by fitting the action potential's upstroke and derivative as it was propagating as a planar front in the two-dimensional monolayer (FK: $\dot{V}_{\max} = 62.0 \text{ V/s}$, $\text{APD}_{90} = 83.0 \text{ ms}$; WS: $\dot{V}_{\max} = 62.0 \text{ V/s}$, $\text{APD}_{90} = 83.0 \text{ ms}$; WS: $\dot{V}_{\max} = 50.0 \text{ V/s}$, $\text{APD}_{90} = 71.0 \text{ ms}$). The cell thickness was assumed to be $16 \mu\text{m}$ and the intracellular conductivity was 6.67 mS/cm . Gap junctions were distributed uniformly around the cell border with nominal coupling strength of 0.1667 mS/cm . If the boundaries of two neighboring cells were closer than $1 \mu\text{m}$ in the cell boundary image, they were connected via a gap junction. Except in the cases where the cell alignments and cell length/width ratio were changed (see Fig. 3), five types of tissues were considered by increasing the number of clefts with constant cell alignments. The cells in these tissues were generated with an elliptical template cell of $120 \mu\text{m}$ in length and $24 \mu\text{m}$ in width. The parameters for the five tissue types are summarized in Table S2. For each type, eight real-

izations of the tissues were produced, to obtain average properties. Sample tissues are shown in Fig. 1 and Fig. S1. The average length, width, and area of cells are summarized in Table S2. All domains were $\sim 7.5 \text{ mm}$ long and 5 mm wide. A 1-ms-long unipolar stimulus, which was two to three times greater than threshold, was applied to initiate propagation. The generated tissue patterns were discretized using the software package Triangle, a Delaunay triangular mesh generator (22). Domains were generated such that the triangle areas did not exceed $50 \mu\text{m}^2$, and no angles in the triangles were $< 28.5^\circ$, except in the triangles at the boundaries (Fig. S2). A typical domain had $\sim 860,000$ nodes. The monodomain model (see Supporting Material for details) was solved using the FEM and Crank-Nicholson method with a time step of $25 \mu\text{s}$ (23). The resultant linear system was solved by the Unsymmetric MultiFrontal method in UMFPACK (24).

RESULTS

Propagation through irregular-shaped cells

Using the tissue generation method described above, domains with different degrees of cell orientation and amount of cleft space were created. Since a tissue was generated from randomly populated elliptical template cells, the simulated tissues contain some holes even when no clefts were intentionally added (Fig. S1, D and G). The placement and shape of each template were controlled by random numbers, enabling the generation of unique cell boundaries even when the tissues were generated from the same parameters (Fig. S1, D–I).

Fig. 1 shows cell boundaries of three sample tissues. Tissue TC0 had no cleft space, mimicking ideal confluent monolayers. In tissues TC2 and TC4, the cleft probabilities were 0.2 and 0.4, respectively. The space between cells increased from TC0 to TC2 and TC4, resulting in smaller contact area between cells. Fig. 1 B shows a histogram of cell-cell contact length. Adding clefts slightly reduced the average of cell-cell contact length and changed the statistical distributions. There is little difference in overall cell size, except that the widths decrease from $28.0 \mu\text{m}$ at TC0 to

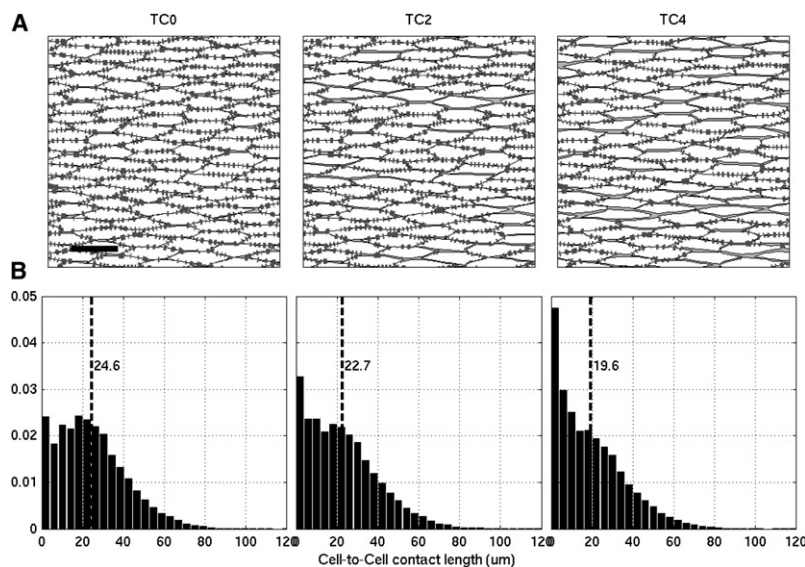


FIGURE 1 (A) Cell boundaries in TC0, TC2, and TC4 tissues. Dark gray indicates gap couplings and light gray indicates extracellular space. Scale bar, $100 \mu\text{m}$. (B) Cell-cell contact length histogram in TC0, TC2, and TC4 tissues. Dashed line indicates the average contact length for each tissue. Because of the model assumption, gap coupling strength is proportional to the cell-cell contact length.

26.1 μm at TC4. The tissue generation parameters, average cell length, width, area, and density in each tissue type, including TC1 and TC3, are shown in Table S2.

Fig. 2 shows the activation patterns generated in the three example tissues arising from a point stimulus at the macroscopic and microscopic levels. At the macroscopic scale, the wavefronts are roughly elliptical in all models. In contrast to a continuous model with uniform and smooth wavefronts, however, the wave in the simulated discrete tissues propagates less regularly at the microscale due to the cell boundaries and distribution of gap junctions. As more cleft space is added, the microscopic fronts become more irregular. The macroscopic conduction velocities in the fast longitudinal direction (LCV) and in the slow transverse direction (TCV) slowed with increasing cleft density. In addition, the conduction velocity anisotropy ratio ($\text{AR} = \text{LCV}/\text{TCV}$) increased as a result of increased microscopic heterogeneity. These effects of the microscopic changes on the CV changes are summarized in Table S3.

Cell geometry and action potential conduction

The increase in AR-CV with increasing cleft space is consistent with the experimental studies of Bursac et al. (1). To further investigate the effects of the microscopic properties on conduction, simulations were performed in which the cell orientations and distribution of clefts were varied as a function of cell length/width ratio (CLWR). Fig. 3 shows the LCV and TCV for various randomly generated tissues as a function of the AR. The simulations were designed to explain the results shown in Fig. 8 of Bursac et al. (1). In each panel, CLWR was changed from 3 to 6 while an average cell area was maintained. Initially, only the cell orientations in the models were varied by changing the cell angle standard

deviation from 0.5 (isotropic, disoriented) to 0.02 (anisotropic, oriented) with zero cleft probability, to mimic confluent tissue. The isotropic, nonaligned tissues are shown to the left of the vertical dashed lines. For the anisotropic tissue with nearly aligned cells (cell angle standard deviation of 0.02), the amount of cleft space was increased by increasing the cleft probability from 0 to 0.4. These tissues are shown to the right of the vertical line. Increasing the alignment of cells in the confluent tissue tended to increase LCV and decrease TCV, thus increasing the AR. Increasing the cleft space, however, acted to decrease both LCV and TCV. The magnitude of the AR-CV transition point corresponding to the inclusion of clefts increased with increasing CLWR. In addition, the maximum and minimum LCV increased and the maximum and minimum TCV decreased with increasing CLWR. Table S4 summarizes the effects of cell geometry on AR and CV.

Gap coupling strength and action potential conduction

Several experimental studies have focused on the effects of modulating gap junction conductance through the application of certain pharmacological agents (25,26). One particular novel antiarrhythmic approach was proposed recently in which the peptide rotigaptide is used to enhance gap junction conductance in infarcted regions to facilitate conduction (25). Unfortunately, precise experimental control of the conductance change is challenging. In the simulation studies, however, it is possible to modify the gap conductance uniformly or nonuniformly. Fig. S3 shows the changes in AR, LCV, and TCV after gap coupling was uniformly increased or decreased from its nominal value in five discrete tissues. LCV and TCV both increased monotonically with

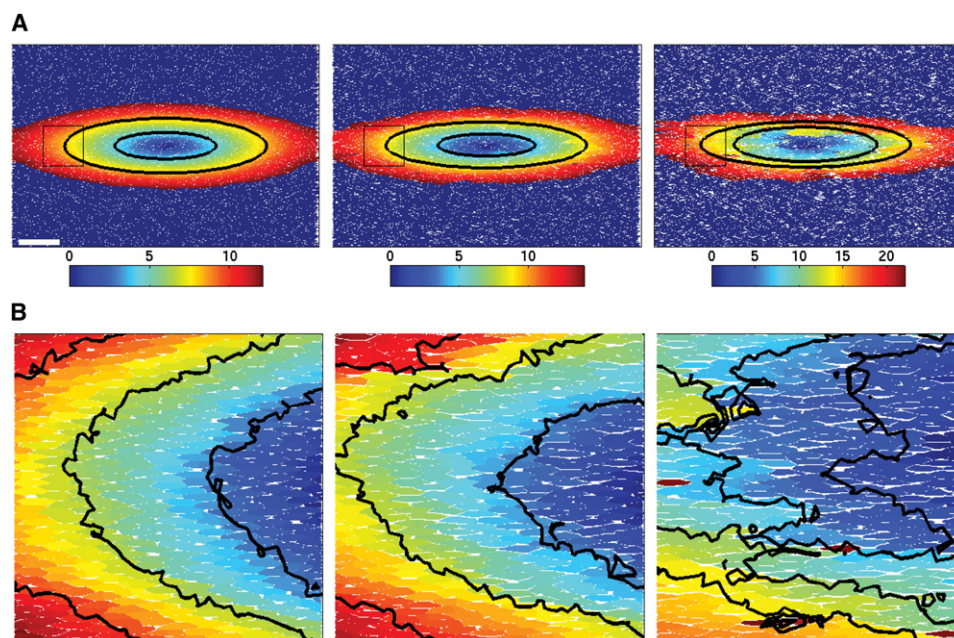


FIGURE 2 (A) Activation time color-map of TC0, TC2, and TC4 tissues at 12, 14, and 22 ms after the stimulus onset. Scale bar, 1 mm. (B) Insets from A, 1×1 mm in area, show detailed isochrones. Interval between isochrones is 1.7 ms in TC0 and TC2 and 2.0 ms in TC4.

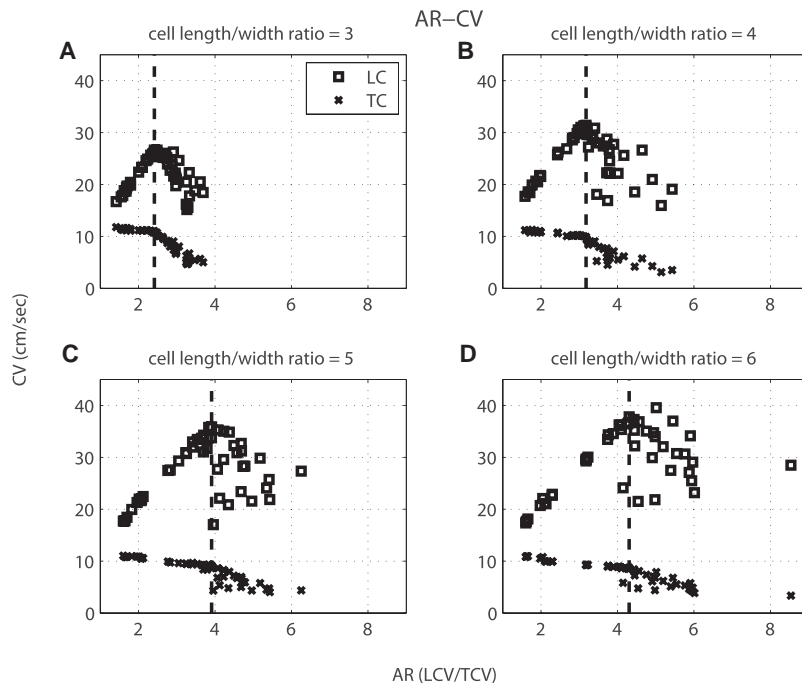


FIGURE 3 AR-CV plot with different cell length/width ratios, cell orientations, and numbers of clefts. The dashed line separates the effects of cell orientations from those of clefts. To the left of the dashed line are changes in AR-CV due to cell orientation, and to the right are changes in AR-CV due to clefts.

increasing gap coupling strength. The AR, however, was not statistically different for any of the gap strengths.

The gap conductance can also be changed nonuniformly. A simulation was performed that compared conduction velocities in tissues with varying degrees of cleft space in which the gap coupling was uniformly increased by 200% for all gap junctions and nonuniformly increased such that the conductance of 50% of the gap junctions was increased 400% and that of the other 50% remained unchanged, for an average gap coupling increase of 200%. A point stimulus was applied at the center of the tissue, and the LCV, TCV, and AR were measured. As shown in Fig. 4, both LCV and TCV were faster for both the uniform and nonuniform gap coupling increase. However, the increase in CV in the case where the gap junction coupling was uniformly increased was greater than that in the case where the gap junction coupling was nonuniformly increased. The uniform case resulted in an average of a 50.7% and 62.4% speed-up in LCV and TCV, respectively, whereas the nonuniform case resulted in an average speed-up in LCV and TCV of 43.3% and 52.2%, respectively. This difference was statistically significant ($p < 0.05$). Although the TCV increase was larger than the LCV increase, the AR decrease was statistically significant for uniform cases and for TC0 and TC1 in nonuniform cases ($p < 0.05$).

Effective tissue conductivities

The changes in conduction velocity and AR were observed with changes in the microscopic parameters governing the cell shape, orientation, and cleft density. One question of interest is how the changes in these parameters affected the

macroscopic conductivities. As noted, the effective tissue conductivity was determined using the global equivalent circuit method and the local subthreshold response method (see Methods). In the global method, the membrane was removed, leaving only the passive intracellular space, and a current was delivered on one edge and grounded at the other edge such that the conductivities could be estimated using Eqs. 3 and 4. In the local method, a subthreshold, intracellular stimulus was applied and the conductivities in both directions were estimated by first determining membrane resistance and then fitting the potential distribution to a continuous passive model. The conductivity estimation methods were first tested using a tissue with rectangular cells of length $120 \mu\text{m}$ and width $24 \mu\text{m}$ for which an analytical solution exists. The methods were tested for three different gap conductances. Table S5 shows the results from the global and local estimation methods. Both methods match the analytical solution very well for the case of uniform tissue of rectangular cells in a regular lattice over the range of gap conductances studied.

Two estimation methods were then applied to the discrete tissues, TC0–TC4, and the result is shown in Fig. 5. In the local method, the passive membrane resistance was estimated to be $9.66 \text{ k}\Omega \cdot \text{cm}^2$ and this value was used for all the tissues. Although there was some difference in the estimation, the correlation coefficients of the two methods are 0.97 and 0.98 for longitudinal and transverse conductivities, respectively. The effective conductivities for the five models were estimated by the global method and are given in Table 1. The results show that both longitudinal and transverse conductivities are negatively correlated with the amount of cleft space.

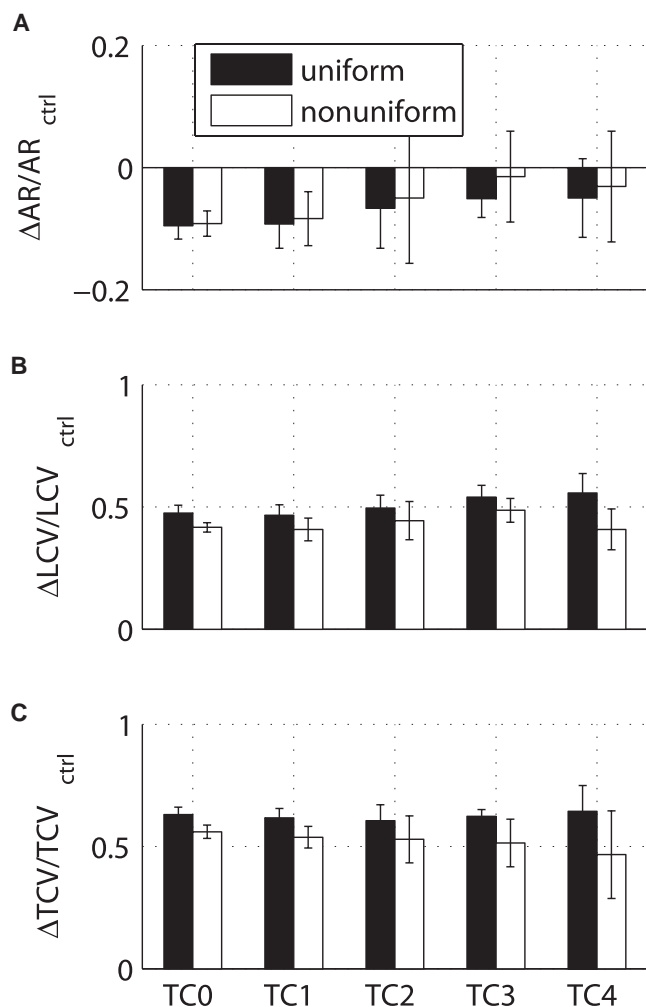


FIGURE 4 Changes in AR and CV after gap coupling increase. Error bar shows standard deviation of changes. Gap coupling strength was increased 200% for all gap junctions in the uniform case and 400% for 50% of gap junctions in the nonuniform case.

The conductivity estimation methods were also compared in a tissue with an abrupt change in cell orientation. In this tissue, cells were aligned in the horizontal direction on the left half and in the vertical direction in the right half. The cleft probability was zero for both halves. Fig. 6 A shows the estimated conductivities in scenarios where 1), the global method was applied only to the left half of the tissue; 2), the local method was applied to several sites along the tissue; 3), the global method was applied to the entire tissue; and 4), the global method was applied only to the right half of the tissue. The estimated conductivities for cases 1, 3, and 4 are 0.85, 0.11, and 0.058, respectively. The results show that the local method estimates a relatively smooth change in conductivity across the transition site, whereas the global method applied across the entire tissue nearly predicts an average conductivity of the two halves ($((0.5(1/0.85 + 1/0.058))^{-1} = 0.11 \text{ mS/cm})$). It is important to note that the local method does a good job of estimating the conductivity

away from the transition site in the right half of the tissue, where the space constant is smaller, than in the left half, where the space constant is larger, and the effect of the boundary on the flow of current is greater.

Effective tissue conductivity and conduction velocity

The changes in macroscopic conductivities due to changes in the microstructure in the discrete tissues suggest that a continuous model with the same macroscopic conductivities could be used to explain the changes of CV seen in Fig. 3. Table 1 gives the effective longitudinal and transverse conductivities of the five models. The inclusion of cleft space reduces not only the effective transverse conductivity, as expected, but also the longitudinal conductivity. This lateral uncoupling causes a slow-down in both the longitudinal and transverse conduction velocities, as shown in Table S3. The effective conductivities for all realizations were then applied to continuous models. Fig. 7 A shows that the ratio of LCVs and TCVs in continuous and discrete models is close to 1 for all the tissues. Fig. 7 B shows that when gap conductance tissues with clefts (TC1, TC2, TC3, and TC4) were increased uniformly such that the effective conductivities of those tissues were identical to those of the confluent tissue, TC0, the LCVs and TCVs were nearly the same. Finally, when the conductivity estimation method was repeated for all the tissues in Fig. 3 whose CV varied with changes in cell length/width ratio, cell orientations, and clefts, the square root of estimated conductivities was linear with CV (correlation efficient 0.995 (Fig. 7 C)), as expected from continuous media theory.

Finally, although the above results support the strong correlation between CV and effective conductivity, the estimation of the conductivities for a continuous model is more challenging to interpret when the properties are not uniform. To investigate this, action potential (AP) propagation was simulated in the domain with an abrupt change in cell orientation (Fig. 6 A). The propagation velocities were plotted from the discrete model and from two continuous models. In one continuous model (model 1), the conductivities were assigned to the values obtained using the global, equivalent circuit method on each half separately. In the other continuous model (model 2), the conductivity was assigned to be smoothly varying based on the estimates obtained using the local, subthreshold response method. When the AP was initiated from the left edge of the tissue, both model 1 and the discrete model showed an abrupt increase in CV near the transition of the change in cell orientation before the CV decreased. In model 2, the CV gradually slowed without an abrupt CV increase (Fig. 6 B). Thus, although the local measurements suggested a smooth change in conductivities, using such tissue properties does not yield behavior that is seen in tissue with an abrupt change in cell orientation. Note that although it appears that the CV fluctuations are

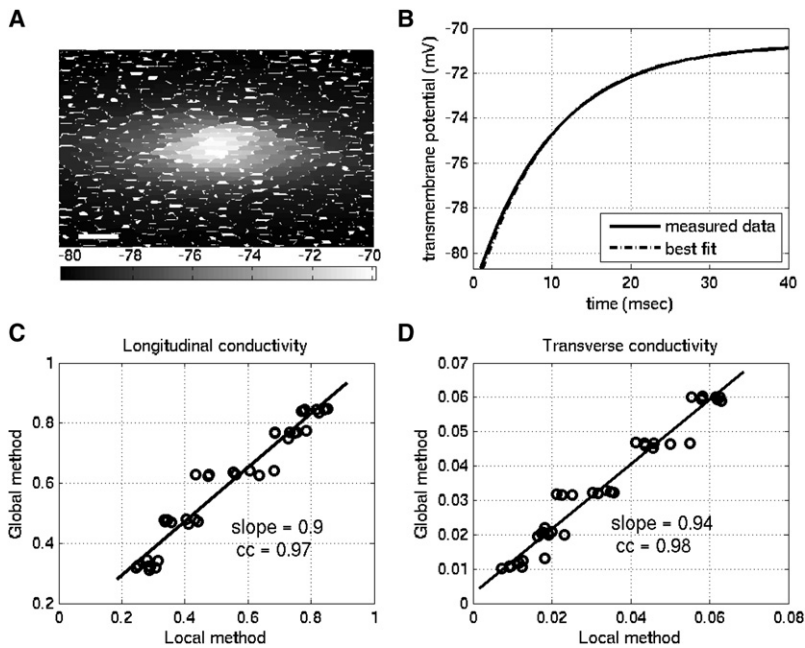


FIGURE 5 (A) Steady-state potential distribution by the subthreshold point stimulus. Scale bar, 200 μm . (B) Time course of membrane potential at the center of the tissue and its best fit with estimate, $R_m = 9.66 \text{ k}\Omega \cdot \text{cm}^2$. (C and D) Global versus local method of estimating effective tissue conductivity in the longitudinal and transverse directions. The solid line is the best linear fit. cc, correlation coefficient.

larger on the left half of the tissue than on the right (Fig. 6 B), a closer examination shows that the size of the fluctuations relative to the average conduction velocity is approximately the same.

DISCUSSION

In this article, we present a new methodology for developing models of cardiac tissue structure that more closely replicates the complex and arbitrary cell shape and orientations found in engineered monolayers. The technique can also be applied to diseased regions like an infarct scar, where there can be significant heterogeneity and sparse, disorganized cell structure (27,28). Because it is straightforward to create different tissue realizations with the same statistical properties, it is possible to perform simulations in a manner consistent with experimental studies where several tissue or heart preparations are used.

One of the key questions addressed in this study is how conduction is influenced by cell orientation and degree of cleft space corresponding mostly to transverse decoupling. Bursac et al. showed that by decreasing the degree of background fibronectin concentration between the micropatterned fibronectin lines, the cells are increasingly elongated and oriented along the lines (1). This results in an increase in longitudinal conduction velocity, a decrease in transverse conduction velocity, and an overall increase in anisotropy ratio of the conduction velocity. As the background fibro-

nectin concentration is further decreased, longitudinal intercellular clefts start to form and then increase in length and number. This results in a further decrease of transverse conduction velocity, along with a slow decrease in longitudinal velocity, which overall yields a further increase in the conduction velocity anisotropy. This increase in structural discontinuity results in a decrease in longitudinal conduction velocity (for $AR > 3.4$), a decrease in transverse conduction velocity, and an overall increase in anisotropy ratio. As shown in Fig. 3, the simulated results were consistent with these experimental findings, as the modeling methodology allows for arbitrarily oriented cells as well as aligned cells with differing amounts of cleft space. The simulated results also show that an AR for which there is a decrease in longitudinal conduction velocity increases with increasing cell length/width ratio.

The results also revealed that in the monolayer, longitudinal conduction velocity can be slowed when there is transverse decoupling. In a previous modeling study, Hubbard and Henriquez showed that in a regular cell structure with no cell overlap, transverse decoupling has no effect on longitudinal conduction (10). In contrast, in a brick wall structure with cell overlap, longitudinal conduction is facilitated by the transverse connections. As a result, a loss of transverse coupling reduces velocity, as seen in the monolayers.

One of the distinct advantages of the computational model is the ability to compute or estimate the effective tissue electrical properties associated with the various tissue structures.

TABLE 1 Effective conductivity obtained by global estimation

	TC0	TC1	TC2	TC3	TC4
σ_L	0.842 (4.2e-3)	0.767 (7.4e-3)	0.632 (7.1e-3)	0.474 (5.7e-3)	0.326 (1.2e-2)
σ_T	0.060 (5.3e-4)	0.046 (6.1e-4)	0.032 (5.0e-4)	0.021 (7.3e-4)	0.011 (1.1e-3)

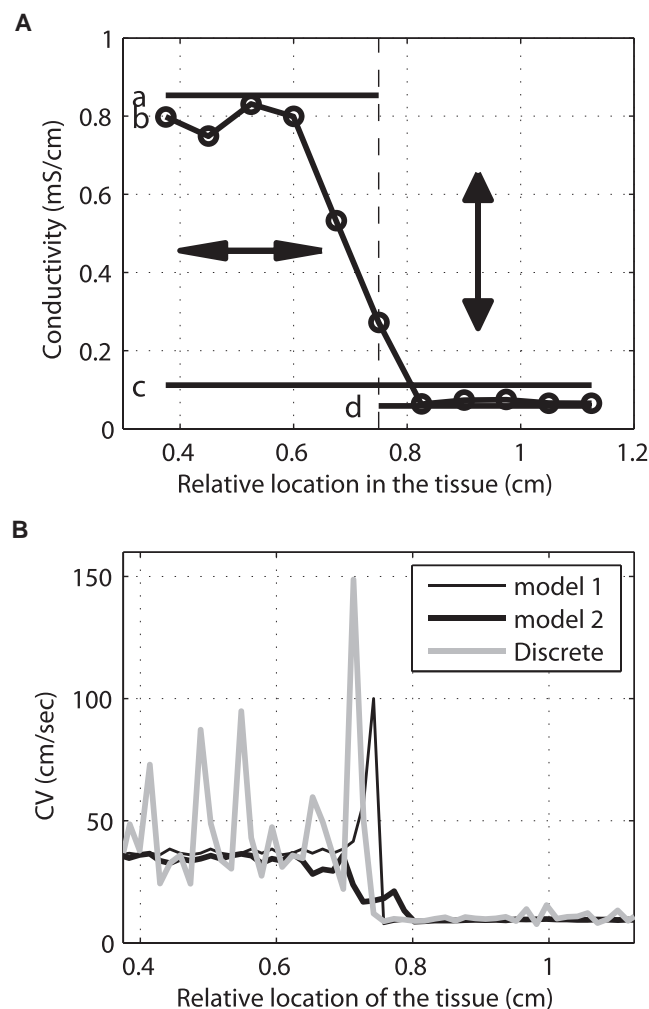


FIGURE 6 (A) Changes in estimated conductivity as a result of changes in cell orientation. The double-headed arrows indicate cell orientations. *a*, Estimated conductivity by the global method applied to only the left half of the tissue. *b*, Estimated conductivity by the local method. *c*, Estimated conductivity by the global method for the whole tissue. *d*, Estimated conductivity by the global method applied to only the right half of the tissue. (B) CV changes of a wavefront moving from the left to the right half of the tissue for the discrete model, the continuous model with conductivities based on the estimates from the local method (model 1), and a continuous model with conductivities on the right and left halves based on the estimates from the global method (model 2).

Using a global estimation method, we show (Fig. 7 *C* and Table 1) that the decrease in longitudinal conduction velocity with transverse decoupling is also associated with a decrease in the effective longitudinal conductivity. In other words, the overlap of cells acts to effectively increase the effective longitudinal conductivity and explains the increase in LCV seen by Hubbard and Henriquez (10) in brick wall models. Because of the ability to consider several realizations of a given tissue, it is possible to obtain statistics regarding the estimates. In general, the greater the degree of transverse decoupling, the greater the variance in the estimates of effective conductivity (Table 1), demonstrating the effects

of small perturbations in microscopic structure on the current flow.

The simulations also showed that the distribution of the coupling strength can affect the conduction velocity. A global uniform increase in gap junction conductance did not lead to the same conduction velocity as did a nonuniform increase in gap junction conductance, even though the average conductance change was the same in both cases. The results showed that the nonuniform gap coupling increase (118% longitudinal and 158% transverse increase in effective conductivity) led to a lower effective conductivity than that resulting from a uniform increase in gap coupling (139% longitudinal and 187% transverse increase in effective conductivity) (Fig. 7, *D* and *E*), and hence a lower conduction velocity (Fig. 4). Although this appears to be surprising, the result is actually expected if the cells are considered as connected in series. Because the gap junctions are in series, the increase in conductance, C , leads to a decrease in resistance, R . For two gap conductances of strength C , the total resistance is ($R = 1/C + 1/C = 2/C$). If the total gap conductance is uniformly doubled from $2C$ to $4C$, the total resistance is halved ($R = 1/2C + 1/2C = 1/C$). If, however, one conductance is unchanged and the other is tripled, such that the total conductance is again doubled to $4C$, the effective resistance is larger than in the uniform case ($R = 1/C + 1/3C = 4/3C$). In the monolayer, the way in which the conductances sum is more complicated, and hence it is not always obvious how a certain distribution of gap junctions will impact the electrical properties. This study shows that the global method properly estimates the changes in conductivity that explain the changes in conduction velocity.

Under the conditions studied, the changes in velocity associated with cell size, orientation, and the distribution and strength of coupling comprising the highly discrete structure could be explained by the corresponding changes in the effective conductivities. Because tissue conductivities require a model to interpret the measurements, two methods were used to determine the values. The first method, which is not applicable under experimental conditions, removed the membrane elements in the model, applied a current through the intracellular space, and evaluated the potential. The effective conductivity is obtained through an estimate of the electric field and the use of Eq. 4. Because the field is applied across the entire tissue, the estimate is an effective global conductivity. The values arising from this method were verified using a simplified tissue structure for which an analytical solution was available. The second method may be experimentally realizable as it uses a subthreshold stimulus response of the tissue and applies a parameter estimation method with a continuous model to determine the effective conductivities. Both estimation methods agreed very well with the analytical solution for the case of regular, rectangular cells (Table S5). Although some small differences were found between the two methods for the discrete tissue with nearly uniform cell orientations and clefts, the

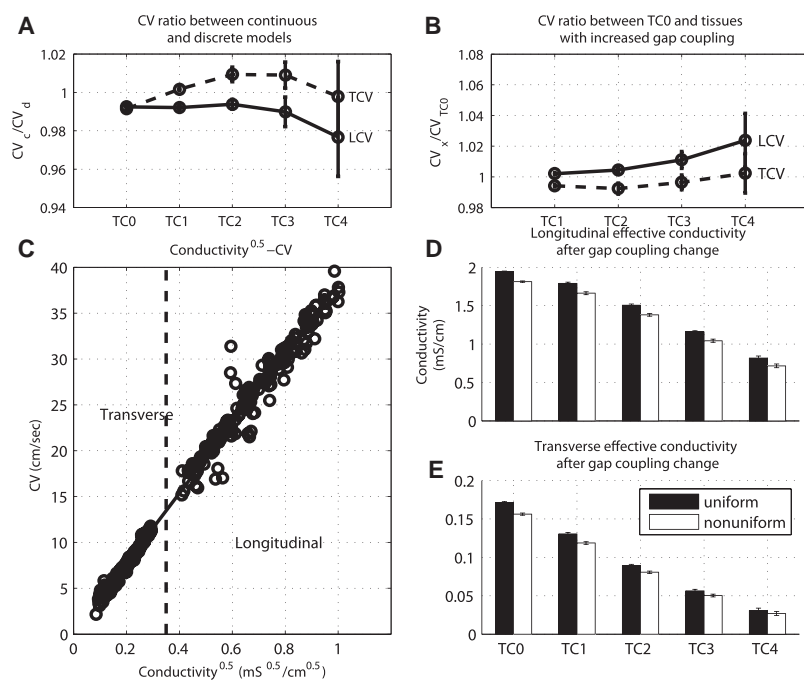


FIGURE 7 (A) CV ratio of the continuous model and the discrete model, whose passive conductivities are identical. (B) CV ratio between TC0 tissue and tissues with increased gap coupling so that their passive conductivities are identical. (C) CV versus square root of conductivity for tissues shown in Fig. 3. All data points are pooled together. Low CV points are from transverse propagation and high CV points are from longitudinal propagation. The line shows the best linear fit, with slope 38.0 and correlation coefficient 0.995. (D) Longitudinal effective conductivity of tissues in Fig. 4. (E) Transverse effective conductivity of tissues in Fig. 4.

estimated conductivities from the two methods showed strong correlation.

The local estimation method did not perform as well with an abrupt change in cell orientation (Fig. 6 A). The local measurement estimates that the conductivity smoothly varies at the transition site. When the smooth conductivities were applied to a continuous model, the resulting conduction velocities and action potential upstrokes near the transition site did not agree with those obtained in the discrete model, as shown in Fig. 6 B. In the discrete model, the CV sharply increased as the wavefront moved from the longitudinally oriented cells to the transversely oriented cells. Note that an abrupt decrease in CV occurred in both the continuous model with abrupt changes in conductivity and the discrete tissue, but not in the continuous model with a smooth change in conductivity and when the wavefront moved in the opposite direction (not shown). This abrupt increase in CV by conductivity changes can be explained by the current/load concept: as the wavefront approaches the boundary, less current flows in the neighboring tissue due to the lower conductivity, and the conduction accelerates (29). Fig. 6 B also shows that the continuous model with abrupt changes in the properties better predicted the behavior of the discrete network. These results suggest that care must be taken when estimating properties in regions with abrupt transitions in fiber orientation or discreteness, particularly when these estimates are being used to construct a continuous model. Note that although the local method may be experimentally realizable, it requires a measurement of the absolute potential distribution over a large area. Although optical methods can be used to assess the distribution, the measurements only reflect relative changes. One approach to overcome this limi-

tation is to calibrate the optical mapping measurements with one-microelectrode measured data, as shown by Pastore et al. (30).

Although the new approach for modeling discrete tissues has made it possible to simulate some phenomena observed in monolayers, a few limitations remain. First, the choice to use cells with relatively fixed geometries led to the emergence of holes in the domain when the cell orientations were random. Such holes are not observed in confluent monolayers, because the cells will spread to fill in the holes (1). In addition, the clefts in the model were generated by shrinking cells laterally, whereas the clefts in vitro result from insufficient expansion of the cells. The model is capable of generating any cell shape, but the ability to create random networks automatically required some compromises. Future studies will consider greater flexibility in the assignment of cell shapes and a tissue generation algorithm that more closely mimics the variety of cell shapes seen in engineered monolayers. It is important to point out that because we assumed a monodomain, the model does not fully account for the effects of tight spaces on conduction (31). The Bueno-Orovio-Cherry-Fenton-Karma model, rather than a detailed ionic-based membrane model, was used to reduce the time of the simulations and to determine its usefulness for performing estimations with experimental data. Although the Bueno-Orovio-Cherry-Fenton-Karma model can reproduce many of the features seen in Hodgkin-Huxley type membrane models, the lack of true ionic currents may limit its utility under some critical regimes of conduction. Note that for the studies of a single wavefront, considered here, the difference between the Bueno-Orovio-Cherry-Fenton-Karma model and more detailed models is

expected to be small. Finally, the studies performed here, and the conclusions derived from the simulations, are based on cells with neonatal distributions of gap junctions. More work is needed to determine how the conclusions generalize to tissues with adult cell shapes and distributions of gap junctions. However, the method can easily be extended to such cases with no modification.

SUPPORTING MATERIAL

Five tables and three figures are available at [http://www.biophysj.org/biophysj/supplemental/S0006-3495\(10\)00135-9](http://www.biophysj.org/biophysj/supplemental/S0006-3495(10)00135-9).

This research was supported by National Institutes of Health Grant No. HL093711-01A2 to C.H.

REFERENCES

- Bursac, N., K. K. Parker, ..., L. Tung. 2002. Cardiomyocyte cultures with controlled macroscopic anisotropy: a model for functional electrophysiological studies of cardiac muscle. *Circ. Res.* 91:e45–e54.
- Fast, V. G., and A. G. Kléber. 1994. Anisotropic conduction in monolayers of neonatal rat heart cells cultured on collagen substrate. *Circ. Res.* 75:591–595.
- Leon, L. J., and B. M. Horáček. 1991. Computer model of excitation and recovery in the anisotropic myocardium. I. Rectangular and cubic arrays of excitable elements. *J. Electrocardiol.* 24:1–15.
- Spach, M. S., and J. F. Heidlage. 1995. The stochastic nature of cardiac propagation at a microscopic level. Electrical description of myocardial architecture and its application to conduction. *Circ. Res.* 76:366–380.
- Spach, M. S., J. F. Heidlage, ..., R. C. Barr. 2000. Electrophysiological effects of remodeling cardiac gap junctions and cell size: experimental and model studies of normal cardiac growth. *Circ. Res.* 86:302–311.
- Carmeliet, E. 1999. Cardiac ionic currents and acute ischemia: from channels to arrhythmias. *Physiol. Rev.* 79:917–1017.
- Cleutjens, J. P., W. M. Blankesteyn, ..., J. F. Smits. 1999. The infarcted myocardium: simply dead tissue, or a lively target for therapeutic interventions. *Cardiovasc. Res.* 44:232–241.
- Li, D., S. Fareh, ..., S. Nattel. 1999. Promotion of atrial fibrillation by heart failure in dogs: atrial remodeling of a different sort. *Circulation.* 100:87–95.
- Spach, M. S., and P. C. Dolber. 1986. Relating extracellular potentials and their derivatives to anisotropic propagation at a microscopic level in human cardiac muscle. Evidence for electrical uncoupling of side-to-side fiber connections with increasing age. *Circ. Res.* 58:356–371.
- Hubbard, M. L., W. Ying, and C. S. Henriquez. 2007. Effect of gap junction distribution on impulse propagation in a monolayer of myocytes: a model study. *Europace.* 9 (Suppl 6):vi20–vi28.
- Leon, L. J., and F. A. Roberge. 1991. Structural complexity effects on transverse propagation in a two-dimensional model of myocardium. *IEEE Trans. Biomed. Eng.* 38:997–1009.
- Shaw, R. M., and Y. Rudy. 1997. Ionic mechanisms of propagation in cardiac tissue. Roles of the sodium and L-type calcium currents during reduced excitability and decreased gap junction coupling. *Circ. Res.* 81:727–741.
- Henriquez, C. S. 1993. Simulating the electrical behavior of cardiac tissue using the bidomain model. *Crit. Rev. Biomed. Eng.* 21:1–77.
- Qu, Z. 2006. Critical mass hypothesis revisited: role of dynamical wave stability in spontaneous termination of cardiac fibrillation. *Am. J. Physiol. Heart Circ. Physiol.* 290:H255–H263.
- Sampson, K. J., and C. S. Henriquez. 2002. Interplay of ionic and structural heterogeneity on functional action potential duration gradients: implications for arrhythmogenesis. *Chaos.* 12:819–828.
- Vigmond, E. J., and L. J. Leon. 1999. Computationally efficient model for simulating electrical activity in cardiac tissue with fiber rotation. *Ann. Biomed. Eng.* 27:160–170.
- Spach, M. S., J. F. Heidlage, ..., P. C. Dolber. 2004. Cell size and communication: role in structural and electrical development and remodeling of the heart. *Heart Rhythm.* 1:500–515.
- Lourakis, M. I. A. 2004. levmar: Levenberg-Marquardt nonlinear least squares algorithms in C/C++. Drexel University, Philadelphia, PA.
- Bueno-Orovio, A., E. M. Cherry, and F. H. Fenton. 2008. Minimal model for human ventricular action potentials in tissue. *J. Theor. Biol.* 253:544–560.
- Fenton, F., and A. Karma. 1998. Vortex dynamics in three-dimensional continuous myocardium with fiber rotation: filament instability and fibrillation. *Chaos.* 8:20–47.
- Wang, L. J., and E. A. Sobie. 2008. Mathematical model of the neonatal mouse ventricular action potential. *Am. J. Physiol. Heart Circ. Physiol.* 294:H2565–H2575.
- Shewchuk, J. R. 2002. Delaunay refinement algorithms for triangular mesh generation. *Comput. Geom. Theory Appl.* 22:21–74.
- Keener, J. P., and K. Bogar. 1998. A numerical method for the solution of the bidomain equations in cardiac tissue. *Chaos.* 8:234–241.
- Davis, T. A., and I. S. Duff. 1997. An unsymmetric-pattern multifrontal method for sparse LU factorization. *SIAM J. Matrix Anal. Appl.* 18: 140–158.
- Hennan, J. K., R. E. Swillo, ..., D. L. Crandall. 2006. Rotigaptide (ZP123) prevents spontaneous ventricular arrhythmias and reduces infarct size during myocardial ischemia/reperfusion injury in open-chest dogs. *J. Pharmacol. Exp. Ther.* 317:236–243.
- Lin, X., C. Zemlin, ..., R. D. Veenstra. 2008. Enhancement of ventricular gap-junction coupling by rotigaptide. *Cardiovasc. Res.* 79:416–426.
- Cabo, C., and P. A. Boyden. 2003. Electrical remodeling of the epicardial border zone in the canine infarcted heart: a computational analysis. *Am. J. Physiol. Heart Circ. Physiol.* 284:H372–H384.
- Gardner, P. L., P. C. Ursell, ..., A. L. Wit. 1985. Electrophysiologic and anatomic basis for fractionated electrograms recorded from healed myocardial infarcts. *Circulation.* 72:596–611.
- Wang, Y., and Y. Rudy. 2000. Action potential propagation in inhomogeneous cardiac tissue: safety factor considerations and ionic mechanism. *Am. J. Physiol. Heart Circ. Physiol.* 278:H1019–H1029.
- Pastore, J. M., S. D. Girouard, ..., D. S. Rosenbaum. 1999. Mechanism linking T-wave alternans to the genesis of cardiac fibrillation. *Circulation.* 99:1385–1394.
- Roberts, S. F., J. G. Stinstra, and C. S. Henriquez. 2008. Effect of nonuniform interstitial space properties on impulse propagation: a discrete multidomain model. *Biophys. J.* 95:3724–3737.